

## ON THE CONTRIBUTION OF THE X-RAY SOURCE TO THE EXTENDED NEBULAR HEII EMISSION IN IZW18

C. KEHRIG<sup>1</sup>, M.A. GUERRERO<sup>1</sup>, J. M. VÍLCHEZ<sup>1</sup>, AND G. RAMOS-LARIOS<sup>2</sup>

<sup>1</sup> Instituto de Astrofísica de Andalucía (IAA-CSIC), Glorieta de la Astronomía s/n, E-18008 Granada, Spain and

<sup>2</sup> Instituto de Astronomía y Meteorología, Dpto. de Física, CUCEI, Universidad de Guadalajara, Av. Vallarta No. 2602, C.P. 44130, Guadalajara, Jalisco, Mexico

*Draft version November 17, 2021*

### ABSTRACT

Nebular HeII emission implies the presence of energetic photons ( $E \geq 54$  eV). Despite the great deal of effort dedicated to understanding HeII ionization, its origin has remained mysterious, particularly in metal-deficient star-forming (SF) galaxies. Unfolding HeII-emitting, metal-poor starbursts at  $z \sim 0$  can yield insight into the powerful ionization processes occurring in the primordial universe. Here we present a new study on the effects that X-ray sources have on the HeII ionization in the extremely metal-poor galaxy IZw18 ( $Z \sim 3\% Z_{\odot}$ ), whose X-ray emission is dominated by a single high-mass X-ray binary (HMXB). This study uses optical integral field spectroscopy, archival Hubble Space Telescope observations, and all of the X-ray data sets publicly available for IZw18. We investigate the time-variability of the IZw18 HMXB for the first time; its emission shows small variations on timescales from days to decades. The best-fit models for the HMXB X-ray spectra cannot reproduce the observed HeII ionization budget of IZw18, nor can recent photoionization models that combine the spectra of both very low metallicity massive stars and the emission from HMXB. We also find that the IZw18 HMXB and the HeII-emission peak are spatially displaced at a projected distance of  $\simeq 200$  pc. These results reduce the relevance of X-ray photons as the dominant HeII ionizing mode in IZw18, which leaves uncertain what process is responsible for the bulk of its HeII ionization. This is in line with recent work discarding X-ray binaries as the main source responsible for HeII ionization in SF galaxies.

*Subject headings:* galaxies: dwarf — galaxies: individual (IZw18) — galaxies: ISM — X-rays: binaries

### 1. INTRODUCTION

The presence of nebular HeII emission points to the existence of a hard radiation field as photon energies  $\geq 54$  eV are necessary to ionize He<sup>+</sup>. Highly ionized systems, like HeII emitters, are expected to be more frequent at high- $z$  (e.g., Cassata, et al. 2013; Mainali, et al. 2018). At the same time, observations of local, HeII-emitting star-forming (SF) galaxies suggest that the lower the metallicity ( $Z$ ), the larger the nebular HeII line intensities (e.g., Guseva, et al. 2000; Senchyna, et al. 2017). This is in line with the harder ionizing stellar spectra predicted at the lower metallicities typical in the early universe (e.g., Tumlinson & Shull 2000); the first, hot metal-free Population III stars produce strong nebular HeII lines (e.g., Yoon, et al. 2012; Visbal, et al. 2015). Still, despite much observational and theoretical effort, including relevant advances in stellar modeling, the source of HeII ionization remains puzzling, especially in metal-poor galaxies (e.g., Eldridge, et al. 2017; Götzberg, et al. 2018; Kehrig, et al. 2018; Stanway & Eldridge 2019; Kubátová, et al. 2019).

There is evidence for enhanced total X-ray luminosities per unit of star formation rate ( $L_X/\text{SFR}$ ) and high-mass X-ray binary (HMXB) populations in extremely metal-poor galaxies ( $Z/Z_{\odot} < 0.1$ ) compared to those of  $\sim Z_{\odot}$  (e.g., Prestwich, et al. 2013; Brorby, et al. 2016; Lebouteiller et al. 2017; Schaerer, et al. 2019; Ponnada, et al. 2020). Furthermore, examples of nearby HeII nebulae associated with HMXBs that appear to act as the only ionizing source are re-

ported (e.g., Garnett et al. 1991; Kaaret, et al. 2004; Gutiérrez & Moon 2014). Thus HMXBs have been proposed as one of the leading mechanisms to ionize He<sup>+</sup> in SF systems. However, it has been recently questioned whether they can provide the required He<sup>+</sup> ionizing flux (e.g., Kehrig, et al. 2018; Senchyna, et al. 2020; Saxena, et al. 2020). Variability of the X-ray source could alleviate this conflict, but so far only the extensive study of the puzzling HeII $\lambda$ 4686-emitting nebula N44C in the LMC considered the effects of an on-off switching X-ray source in time periods of years (see Nazé, et al. 2003).

IZw18 is among the most metal-poor ( $12+\log(\text{O}/\text{H}) = 7.11 \sim 3\%$  solar<sup>1</sup>; e.g., Kehrig et al. 2016, K16) HeII-emitting SF galaxies known at  $z \sim 0$ . It thus can be considered a nearby analog of distant metal-poor HeII emitters, providing a unique laboratory to study the high-ionization phenomenon expected to be common in the reionization era. Based on integral field spectroscopy (IFS) data, Kehrig, et al. (2015, K15) unveiled the entire nebular HeII $\lambda$ 4686-emitting region in IZw18 with a diameter of  $\approx 5''$  ( $\approx 440$  pc at the distance of 18.2 Mpc; Aloisi et al. 2007). K15 found that only peculiar hot (nearly) metal-free massive stars could explain the HeII ionization in IZw18 (see also Kehrig, et al. 2018, K18). The main goal of this Letter is to investigate in detail the spatial correlation between the HeII emission in IZw18 and its single HMXB (Thuan et al. 2004, T04), the vari-

<sup>1</sup> Assuming a solar metallicity  $12+\log(\text{O}/\text{H})_{\odot} = 8.69$  (Asplund et al. 2009)

ability of the latter on short (days) and long (decades) timescales and its expected  $\text{He}^+$  ionizing photon production to assess the contribution of the X-ray emission to the nebular  $\text{HeII}\lambda 4686$  ionization.

## 2. OBSERVATIONS

This study combines archival X-ray and Hubble Space Telescope (HST) observations with IFS data.

The IFS observations of IZw18, obtained on 2012 December, use the Potsdam Multi-Aperture Spectrophotometer (PMAS; Roth et al. 2005) at the Calar Alto Observatory (Spain). PMAS provides a field of view (FOV) of  $16'' \times 16''$  with a sampling of  $1'' \times 1''$  over  $\sim 3640\text{--}7200$  Å (see K15,K16 for details). The data have been used to obtain a continuum-subtracted spectral map of the nebular  $\text{HeII}\lambda 4686$  emission line in IZw18.

IZw18 has been targeted by most modern X-ray observatories, including ROSAT, Chandra, XMM-Newton and Swift. Table 1 lists the details of these X-ray observations. The Chandra and XMM-Newton data were reprocessed using the specific reduction packages Chandra Interactive Analysis of Observations (CIAO v4.9, Fruscione et al. 2006) and XMM-Newton Science Analysis System (SAS v17.0, Gabriel et al. 2004), respectively. The ROSAT and Swift datasets were processed using generic HEASARC reduction packages. IZw18 is detected as a point source in all these observations except in the Chandra observations, with the highest spatial resolution ( $\approx 0''.5$ ) among the available X-ray data, which suggest faint extended emission toward the south (T04). Table 1 provides the count rates of these detections, which are below a  $3\sigma$  threshold in the shortest Swift observations.

We also use archival HST images of IZw18. The location of the hot, young massive stars is probed using the HST STIS image obtained through the far-UV filter F25SRF2 with  $\lambda_c = 1457$  Å (PI:T.M. Brown, prop. 9054, Brown et al. 2002). The HST WFPC2/F658N image (PI:E. Skillman, prop. 6536, de Mello et al. 1998) outlines the ionized gas emission in the  $\text{H}\alpha$  line.

## 3. DATA ANALYSIS

### 3.1. UV, optical and X-ray Imaging

Previous analyses of the spatial properties of the X-ray emission in IZw18 were presented by T04 using the same Chandra data set used here. They suggested the presence of an HMXB spatially coincident with the bright northwest (NW) SF knot of IZw18 and a fainter diffuse emission toward the south. To investigate the spatial distribution of the X-ray emission from IZw18, we have produced images in the soft 0.3-1.2 keV, medium 1.2-2.5 keV, hard 2.5-8.0 keV, and broad 0.3-8.0 keV X-ray bands using the ACIS subpixel event resolution capability, with subpixel size  $1/4$  their natural size of  $0''.5$ . Images were subsequently convolved with subpixel PSF images of the same energy and adaptively smoothed with a Gaussian kernel size between  $0''.5\text{--}2''.0$ .

To spatially correlate the different components of IZw18, we compare in detail the distribution of the emission of X-ray with that of the hot young massive stars and ionized gas from HST images, and with the PMAS  $\text{HeII}\lambda 4686$  map. The HST and Chandra images were registered using USNO stars in their FoV. As noted by T04,

the astrometric accuracy of the Chandra observations is  $\approx 0''.5$  due to the limited number of optical counterparts of X-ray sources. Similarly, the HST images and PMAS  $\text{HeII}\lambda 4686$  map were registered using the HST image and PMAS map in the  $\text{H}\alpha$  emission line. Their relative registration accuracy is estimated to be within  $\approx 0''.5$ .

Figure 1 (left) presents a color-composite picture of the soft, medium, and hard X-ray band images. This image confirms the presence of a hard X-ray point source at the position of the NW knot (T04) and reveals that the diffuse emission toward the south is redder, i.e., the diffuse emission is softer than the point source. Figure 1 (center) shows that the HMXB emission (blue) is coincident with the young massive stellar cluster (green) centered in the NW component of  $\text{H}\alpha$  emission (red) of IZw18. The diffuse X-ray emission extends south, along some holes in the  $\text{H}\alpha$  emission. Figure 1 (right) displays the extended nebular  $\text{HeII}\lambda 4686$ -emitting gas showing, for the first time, that the  $\text{HeII}\lambda 4686$  emission peak is displaced  $\approx 2''.5$  ( $\approx 200$  pc projected at the distance of 18.2 Mpc) from the south of the HMXB in IZw18. The  $\text{HeII}$  emission overlaps part of the much more extended  $\text{H}\alpha$  emission, whose peaks appear noncoincident (see also Figure 2 (middle) panels from K15).

### 3.2. X-ray Variability

We used the different X-ray datasets listed in Table 1 to extract X-ray spectra utilizing apertures encompassing the X-ray emission associated with the NW SF knot. Background spectra were extracted from nearby source-free regions. The source and background spectra were then processed to obtain calibration files. The background-subtracted ROSAT/PSPC, Chandra/ACIS-I, and XMM-Newton/EPIC X-ray spectra of IZw18 are shown in Figure 2. The Swift spectra are not shown given their limited count number.

Previous analyses of the X-ray spectrum of the IZw18 HMXB considered plasma emission and power-law models for ROSAT (Martin 1996) and Chandra data (T04), and power-law and thin accretion disk around a Kerr black hole (BH) models for the XMM-Newton data obtained on 2002 April 10 (2002-04-10-XMM-Newton; Kaaret & Feng 2013). The latter model is the most specific for HMXBs, but too complex for the quality of some of the available datasets. To preserve the consistency of the investigation of the HMXB X-ray variability, a power-law model will be used for all datasets. For the fit, a fixed Galactic extinction along the line of sight of IZw18 consistent with a hydrogen column density ( $N_{\text{H}}$ ) of  $2.9 \times 10^{20} \text{ cm}^{-2}$  (HI4PI Collaboration 2016) is assumed. An additional absorption component with the same chemical abundance as IZw18 is adopted to describe the local absorption.

The results of our spectral modeling are summarized in Table 2. We first started modeling the 2002-04-10-XMM-Newton spectra, which have the largest count number. The power-law model (black, blue, and green histograms in Figure 2) results in an acceptable fitting ( $\chi^2/\text{DoF}=1.33$ ). The best-fit power-law photon index  $\Gamma=1.95$  is typical of synchrotron emission, whereas the  $N_{\text{H}}$  of the local component ( $=3.6 \times 10^{21} \text{ cm}^{-2}$ ) is consistent with that derived by Lelli et al. (2012) at the location of the X-ray source. We then fitted the XMM-Newton/EPIC spectra extracted from the observations

TABLE 1  
X-RAY OBSERVATIONS OF IZw18

X-ray Observatory	Instrument	Data set	Date	Net Exposure Time (ks)	Count Rate <sup>a</sup> (ks <sup>-1</sup> )
ROSAT	PSPC	rp600165n00	1992 04 30	16.2	7.2±0.7
Chandra	ACIS-I	600108	2000 02 08	31.0	12.3±0.6
XMM-Newton	EPIC-pn	0112520101	2002 04 10	24.2	90.4±2.0
	EPIC-MOS1			31.1	28.3±1.0
	EPIC-MOS2			30.9	28.4±1.0
XMM-Newton	EPIC-pn	0112520201	2002 04 16	5.4	76.9±4.0
	EPIC-MOS1			10.4	26.8±1.7
	EPIC-MOS2			10.4	29.2±1.7
Swift	XRT	00040765001	2011 03 25	2.0	2.1±1.1
Swift	XRT	00040765002	2011 03 29	0.9	6.6±2.8
Swift	XRT	00040765003	2012 03 23	0.4	9.2±5.0
Swift	XRT	00040765004	2012 03 26	0.3	8.9±5.6
Swift	XRT	00040765005	2012 08 29	2.6	6.7±1.6

(a) Count rates are computed within the nominal energy bands of each X-ray observatory: ROSAT/PSPC (0.1-2.4 keV), Chandra/ACIS-I (0.3-10.0 keV), XMM-Newton/EPIC (0.3-10.0 keV), and Swift/XRT (0.2-10.0 keV).

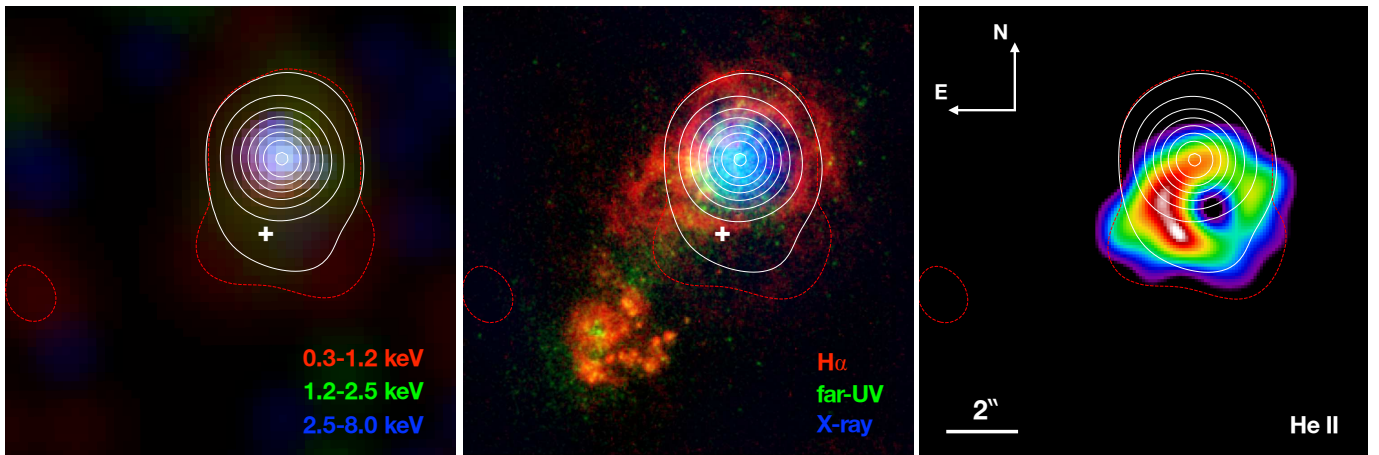


FIG. 1.— Multiwavelength images of IZw18 and Chandra ACIS-I X-ray contours. (Left panel) Color-composite Chandra ACIS-I X-ray picture in the soft 0.3-1.2 keV (red), medium 1.2-2.5 keV (green), and hard 2.5-8.0 keV (blue) energy bands. (Center panel) Color-composite optical HST WFPC2/F658N H $\alpha$  emission line (red), HST STIS/FUV/F25SRF2 continuum at 1457 Å (green), and X-ray Chandra ACIS-I 0.3-8.0 keV (blue) picture. (Right panel) PMAS map of nebular HeII $\lambda$ 4686 emission. In this map, the pixel scale has been regridded to 0''.1 applying a 2D linear interpolation, and then smoothed at the original pixel scale using a  $\sigma=1''$  Gaussian kernel; intensity is presented in the square root scale. The orientation, FoV, and scale of the three panels match each other. The HeII emission peak in the right panel is marked by a '+' symbol in the left and central panels. The white contours correspond to the PSF of the X-ray point source, and display the intensity of the 0.3-8.0 keV X-ray emission using a logarithmic scale from a  $3\sigma$  level to the intensity peak; the red contour shows the  $3\sigma$  level of the soft 0.3-1.2 keV emission. The nominal FWHM of the Chandra ACIS PSF,  $\approx 0''.5$ , is in between the first and second highest white contours, whereas the HeII emission peak is observed well outside the latter.

on 2002 April 16, using a similar absorbed power-law model. The spectra have lower quality than those obtained just 6 days before given their shorter net exposure times, but the parameters of the best-fit models are consistent within their uncertainties with those obtained for the 2002-04-10-XMM-Newton observations (see Table 2).

Next we proceed to fit the ROSAT/PSPC and Chandra/ACIS-I spectra with this same absorbed power-law model. The parameters of the best-fit models (black histograms in the top panels of Figure 2) are notably different from those obtained for the XMM-Newton/EPIC spectra. As for the ROSAT/PSPC spectrum, the data quality is not adequate to reliably constrain the model parameters (see their  $1\sigma$  uncertainties in Tab. 2) and indeed the scaled best-fit model of the 2002-04-10-XMM-Newton spectra (purple histogram in the top left panel of Figure 2) is consistent with the ROSAT/PSPC spec-

trum. On the other hand, the Chandra ACIS-I spectrum is much softer than the scaled best-fit model of the 2002-04-10-XMM-Newton spectra (purple histogram in the top right panel of Figure 2), i.e., the internal extinction during the Chandra observation was much lower than that during the XMM-Newton observations. The Chandra spectrum also implies the lowest  $L_X$ . Finally, we have adopted the best-fit model of the 2002-04-10-XMM-Newton spectra to derive the  $L_X$  from the count rate of the Swift observations. These are listed in Table 2, where the uncertainties are derived from the  $1\sigma$  error bar of the count rate.

The long-term evolution of  $L_X$  in the energy band 0.5-8.0 keV ( $L_{X,0.5-8 \text{ keV}}$ ; see Table 2) is shown in the upper panel of Figure 3. Apparently, the IZw18 HMXB switches from a low state with  $L_{X,0.5-8 \text{ keV}}$  a few times  $10^{39} \text{ erg s}^{-1}$  to an upper state with  $L_{X,0.5-8 \text{ keV}}$  of ( $1-$

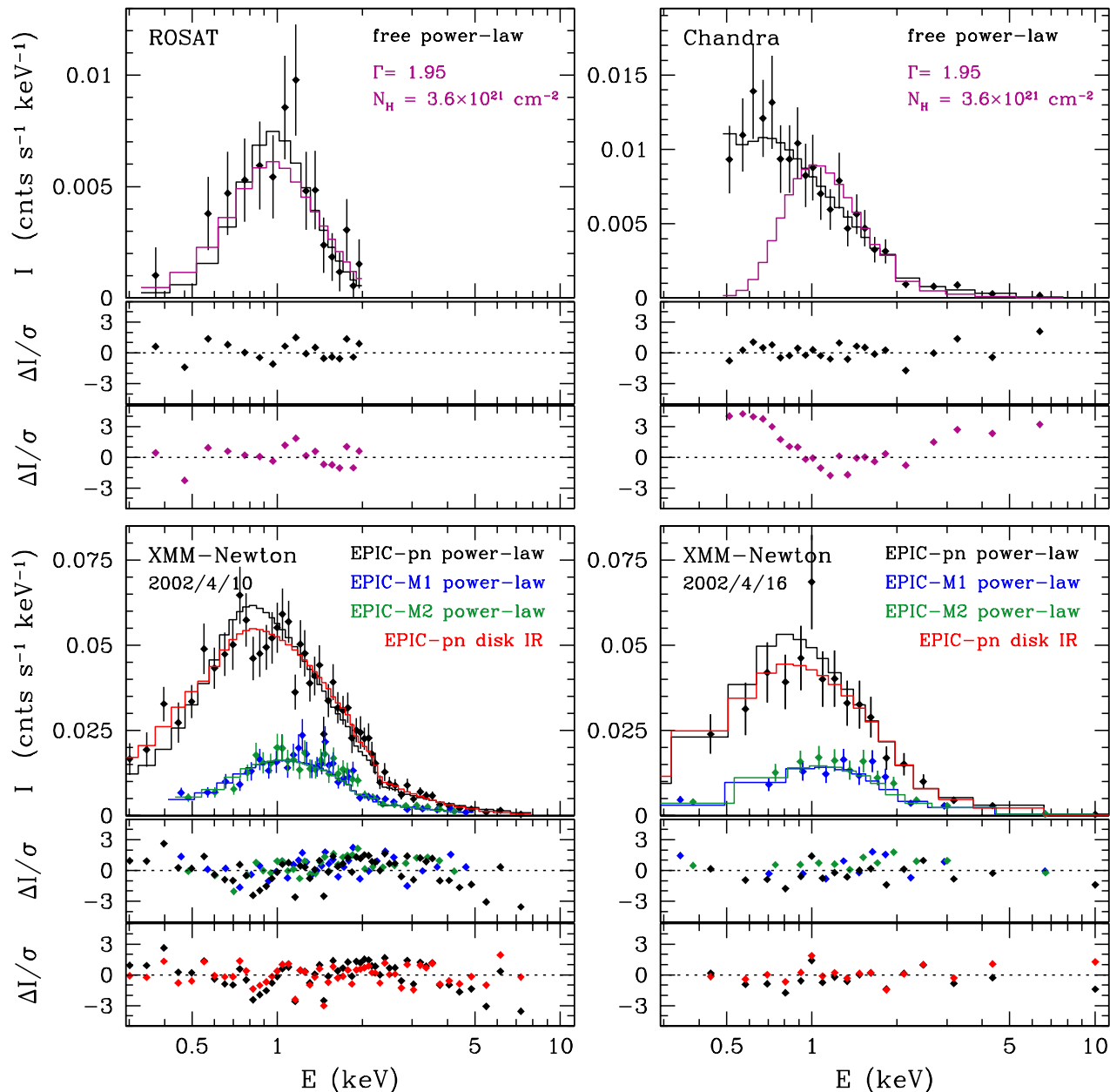


FIG. 2.— Background-subtracted ROSAT (top left), Chandra (top right), and XMM-Newton (bottom) X-ray spectra of IZw18 (points) overplotted by best-fit models (histograms). The error bars of each data point correspond to  $1\sigma$  statistical uncertainties. The best-quality XMM-Newton spectra are fitted using an absorbed power law (black for EPIC-pn, blue for EPIC-MOS1, and green for EPIC-MOS2). An absorbed irradiated disk model is also shown for the EPIC-pn spectrum (red). The ROSAT and Chandra spectra are fitted using an absorbed power law models (black), with the scaled best-fit power law model of the 2002-04-10-XMM-Newton observations also overplotted (purple). Lower panels show the residuals of the best-fit models where the data points' colors correspond to those of the best-fit models.

$2) \times 10^{40}$  erg  $s^{-1}$ . These high  $L_X$  and spectral changes are consistent with those of ultraluminous X-ray sources, as discussed by Kaaret & Feng (2013), although T04 argued that HMXBs in low metallicity galaxies tend to have higher  $L_X$ . The transition from one state to the other occurs in timescales shorter than 2-3 yr, as suggested by the increase in luminosity from the Chandra to the XMM-Newton observations, and from the different Swift observations, although the latter are affected by large uncertainties in the luminosity estimates.

The short-term variability is shown in the lower panels of Figure 3. Lightcurves in the energy band 0.5-8.0 keV with a bin size of 4.0 and 1.2 ks have been extracted

from the Chandra/ACIS-I and XMM-Newton/EPIC-pn observations, respectively. The count rates and their  $1\sigma$  uncertainties have been converted to X-ray luminosities using the average  $L_{X,0.5-8 \text{ keV}}$  at each epoch given in the last column of Table 2. For each data set, the X-ray emission is mostly consistent with its mean value, which may be suggesting small fluctuations. In this sense, the X-ray level of the two XMM-Newton observations, obtained  $\sim 6$  days apart, are mostly consistent with each other.

This leads us to conclude that the IZw18 HMXB has a relatively constant emission in short (hours to days) timescales, with variations of factors of only a few in longer (a few years) timescales. There are hints that the

TABLE 2  
X-RAY SPECTRAL FITTINGS AND LUMINOSITIES OF IZw18

X-ray Observatory and Instrument	Date	$N_{\text{H}}$ ( $10^{21} \text{ cm}^{-2}$ )	$\Gamma$	$\chi^2/\text{DoF}$	$f_{0.3-2.4\text{keV}}$ ( $10^{-14} \text{ erg cm}^{-2} \text{ s}^{-1}$ )	$f_{0.5-8.0\text{keV}}$ ( $10^{-14} \text{ erg cm}^{-2} \text{ s}^{-1}$ )	$L_{0.3-2.4\text{keV}}$ ( $10^{38} \text{ erg cm s}^{-1}$ )	$L_{0.5-8.0\text{keV}}$ ( $10^{38} \text{ erg cm s}^{-1}$ )
ROSAT PSPC <sup>a</sup>	1992 04 30	$16^{+34}_{-5}$	$4.2^{+4.3}_{-2.0}$	12.7/14 = 0.91	3.8	6.5	$400^{+20}_{-150}$	$127^{+6}_{-60}$
		3.6	1.95	16.5/16 = 1.03	7.5	8.9	$30.0^{+4.2}_{-3.3}$	$35.5^{3.8}_{-4.4}$
Chandra ACIS-I	2000 02 08	$0.5^{+1.3}_{-0.5}$	$1.96^{+0.28}_{-0.21}$	15.2/20 = 0.76	3.7	6.3	$19.4^{+0.8}_{-1.5}$	$26.9 \pm 2.1$
XMM-Newton EPIC	2002 04 10	$3.6 \pm 0.6$	$1.95 \pm 0.07$	158.7/122 = 1.33	13.5	28.0	$94.3 \pm 1.5$	$131.2^{+1.9}_{-4.0}$
XMM-Newton EPIC	2002 04 16	$3.2^{+1.1}_{-0.9}$	$1.84 \pm 0.13$	33.6/38 = 0.88	12.1	26.8	$48.4 \pm 2.1$	$107.2 \pm 4.4$
Swift/XRT	2011 03 25	3.6	1.95	...	4.5	9.2	$31 \pm 17$	$44 \pm 23$
Swift/XRT	2011 03 29	3.6	1.95	...	14	29	$98 \pm 42$	$135 \pm 60$
Swift/XRT	2012 03 23	3.6	1.95	...	20	41	$135 \pm 70$	$190 \pm 100$
Swift/XRT	2012 03 26	3.6	1.95	...	19	39	$130 \pm 80$	$180 \pm 110$
Swift/XRT	2012 08 29	3.6	1.95	...	14	30	$98 \pm 23$	$138 \pm 33$

(a) First and second rows show the results of ROSAT spectral modeling based on a free power-law fit and using the best-fit model of the 2002-04-10-XMM-Newton spectrum, respectively.

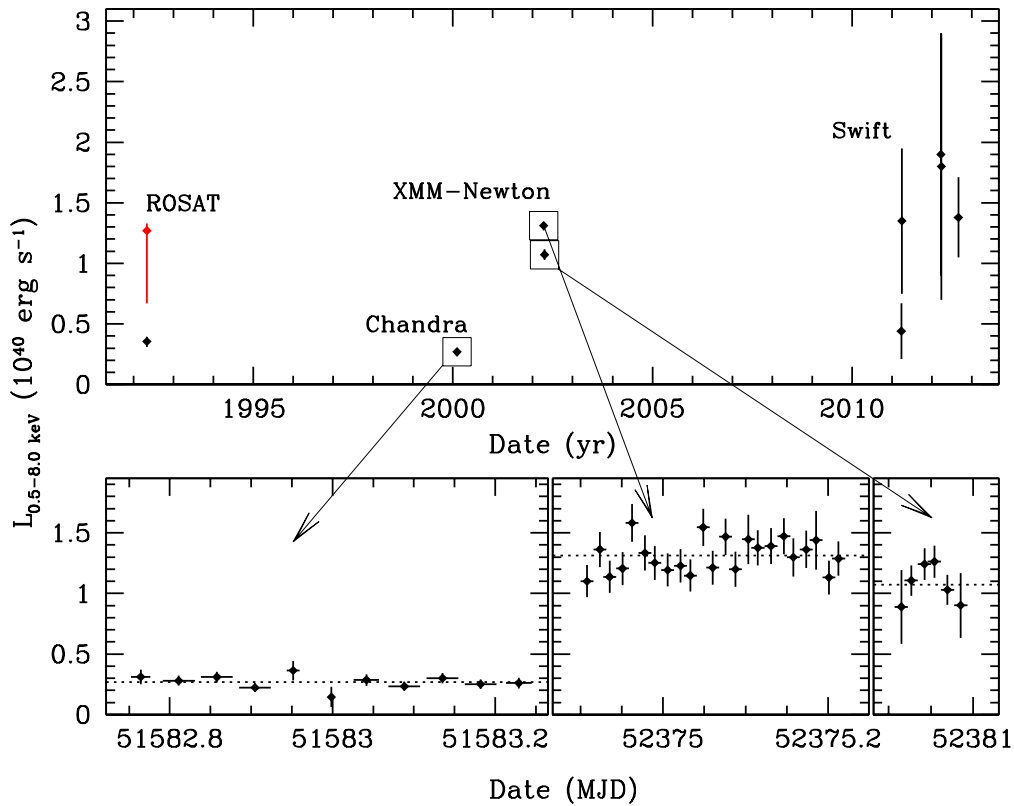


FIG. 3.— Long-term (top) and short-term (bottom) X-ray variability of the X-ray emission from IZw18. The intrinsic  $L_{\text{X},0.5-8 \text{ keV}}$  and corresponding error bars are derived from the models detailed in Table 2. The ROSAT red data point corresponds to a free power-law fit, whereas the black data point uses the best-fit parameters of the fit to the 2002-04-10-XMM-Newton spectrum. The bottom panels present expanded light-curves of the Chandra and XMM-Newton observations. The dashed horizontal lines in these panels correspond to the average X-ray luminosities during the observations.

larger X-ray fluxes are associated with an increase of  $N_{\text{H}}$  toward this source, as typically seen in X-ray sources fed by accretion such as HMXBs.

#### 4. DISCUSSION

The nebular HeII $\lambda$ 4686 emission observed in some SF galaxies has often been attributed to X-ray emission from HMXBs (e.g. Thuan & Izotov 2005; Schaerer, et al. 2019). This hypothesis has been critically tested by Senchyna, et al. (2020, S20) using photoionization grids accounting for the combined contribution of HMXBs

and young massive stars for metallicities from  $Z=0.02$  to  $Z=0.001$  ( $\simeq 5\%$  solar), and provide predictions for the HeII/H $\beta$  ratio that correspond to a range of values of the  $L_{\text{X},0.5-8 \text{ keV}}/\text{SFR}$  ratio. We estimate a SFR of  $0.14 M_{\odot} \text{ yr}^{-1}$  for IZw18<sup>2</sup> based on its  $L(H\alpha)=1.73 \times 10^{40} \text{ erg s}^{-1}$  (K16) and the widely used  $\text{SFR}-L(H\alpha)$  relation from Kennicutt (1998). Therefore, taking the  $L_{\text{X},0.5-8 \text{ keV}}$  value in Table 2 derived from the

<sup>2</sup> The IZw18 integrated  $F(H\alpha)=4.36 \times 10^{-13} \text{ erg s}^{-1} \text{ cm}^{-2}$  (K16) was translated to  $L(H\alpha)$  assuming a distance of 18.2 Mpc.

2002-04-10-XMM-Newton data set, this implies an observed  $L_{X,0.5-8 \text{ keV}}/\text{SFR}$  of  $9 \times 10^{40} \text{ erg s}^{-1}/(M_{\odot} \text{ yr}^{-1})$ . According to S20's predictions, this  $L_{X,0.5-8 \text{ keV}}/\text{SFR}$  value results in  $\text{HeII}/\text{H}\beta$  between 0.0004 to 0.0025, regardless of the metallicity assumed in the models, a value well below the observed  $\text{HeII}/\text{H}\beta$  of  $0.023 \pm 0.004$  in IZw18 (K16). To reinforce this result, we have computed the total HeII-ionizing photon flux  $Q(\text{HeII})$  from Kerr BH and irradiated disk models of the X-ray emission detected in the 2002-04-10-XMM-Newton observation. The thin accretion disk around a Kerr BH model including a Comptonization component provides an extrapolation to UV wavelengths  $< 228 \text{ \AA}$  similar to that of the multicolor disk models used by S20. The best fit for this model has very similar parameters to those reported by Kaaret & Feng (2013), with an acceptable fitting quality ( $\chi^2/\text{DoF}=0.90$ ). The intrinsic (unabsorbed)  $\log Q(\text{HeII})$  for this model is  $\approx 48.4 \text{ photon s}^{-1}$ , i.e.,  $\approx 50$  times lower than that of  $\log Q(\text{HeII})=50.1 \text{ photon s}^{-1}$  reported by K15. Meanwhile, the emission model of a disk irradiated by the Compton tail (Gierliński et al. 2009) is of particular interest, as the physical processes of disk irradiation provide a meaningful description of the expected UV spectrum to constrain more reliably  $Q(\text{HeII})$  (Berghea & Dudik 2012). The best fit for this model has a slightly better fit quality ( $\chi^2/\text{DoF}=0.93$ ) with a local  $N_{\text{H}}=1.5 \pm 0.8 \times 10^{21} \text{ cm}^{-2}$ , inner disk temperature  $0.55 \pm 0.25 \text{ keV}$ , photon index  $2.9 \pm 0.6$ , and irradiated flux fraction of 2.3% for the (other parameters were fixed at typical values according to; Gierliński et al. 2009). The resulting intrinsic (unabsorbed)  $\log Q(\text{HeII})$  is  $\approx 49.1 \text{ photon s}^{-1}$ , which is still 10 times lower than observed. It is worthwhile noting that the  $L_X$  derived from these models is very similar to that derived from a power-law model.

Furthermore, the HMXB is coincident with the NW stellar cluster of IZw18, whereas the nebular HeII emission (diameter  $\approx 440 \text{ pc}$ ) shows a shell-like structure extending south of the HMXB; a  $\approx 2.''5$  (200 pc) offset is observed between the HeII emission peak and the HMXB (see Section 3.1). Interestingly, the diffuse X-ray emission to the south of the HMXB delineates the southernmost edge of the HeII emission. A spectral analysis of this diffuse emission is not feasible, but its photon median energy,  $\approx 0.7 \text{ keV}$ , is consistent with that found in superbubbles (e.g., DEM L152 in the LMC; Jaskot et al. 2011). The ‘‘true’’ spatial distribution of the diffuse X-ray emission might certainly fill the cavity of ionized gas suggested by its HeII and  $\text{H}\alpha$  emission, but the bright X-ray emission from the HMXB prevents the detection of its northern rim. Assuming that the X-ray-emitting plasma responsible of the diffuse emission had similar temperature as that of the typical superbubble DEM L152 (0.37 keV; Jaskot et al. 2011), the count rate from the diffuse emission of  $0.39 \pm 0.11 \text{ counts ks}^{-1}$  ( $\sim 30$  times smaller than that of the HMXB) implies  $L_{X,0.5-8 \text{ keV}} \sim 10^{38} \text{ erg s}^{-1}$ . This  $L_X$  is consistent, at the high end, with that of LMC superbubbles (Dunne et al. 2001). The  $Q(\text{HeII})$  of this diffuse soft X-ray emission is at least 4 orders of magnitude lower than that of the hard X-ray point source.

Contrary to our results, previous studies claim that emission from the hard X-ray point source

in IZw18 may be significant for its HeII ionization (e.g., Lebouteiller et al. 2017; Heap et al. 2019; Schaerer, et al. 2019). Lebouteiller et al. (2017) and Heap et al. (2019), however, do not consider the nebular HeII budget in their modeling, which is key to studying the origin of the bulk of the HeII ionizing photons (see, e.g., K15; K18; Kehrig et al. 2020). On the other hand, Schaerer, et al. (2019) assume that the nebular HeII emission in IZw18 is fully ionized by its HMXB, this way overlooking the energy-dependent cross section of  $\text{He}^+$  which must be considered for the estimation of the intrinsic X-ray ionizing power (see above). Moreover, these works do not take into consideration the distinct spatial locations of the X-ray and the HeII emissions in IZw18 unveiled here.

## 5. SUMMARY AND CONCLUDING REMARKS

Cosmic dawn marks a phase transition of the universe during which Population III-stars and their hosts put an end to the dark ages. The nature of these first sources is highly unconstrained. The hard spectra of Population III and nearly  $Z=0$  stars can produce intense HeII emission. However, the origin of nebular HeII emission in metal-poor SF galaxies, near and far, is still unclear (e.g., K18; Saxena, et al. 2020).

IZw18 is a very-metal-poor ( $Z \sim 3\% Z_{\odot}$ ), HeII-emitting SF system, which is a unique local laboratory for probing the conditions dominating in distant HeII emitters. Here we combine optical IFS observations with archival HST and X-ray data of IZw18 to obtain a new view on the effects of X-ray photons on its nebular HeII-ionization.

We confirm the previously reported HMXB which dominates the IZw18 X-ray emission, although a softer diffuse emission is also present. The observation period covered by the X-ray datasets allows us to study the X-ray variability of the IZw18 HMXB for the first time. Its  $L_{X,0.5-8 \text{ keV}}$  is unchanging in hours-days while it can vary by factors of a few in time-scales of years. There is thus no observational evidence for episodes of highly enhanced X-ray emission that, eventually, could power the HeII emission in IZw18.

We find that the best-fit Kerr BH and irradiated disk models yield, respectively,  $Q(\text{HeII}) \sim 50$  and 10 times lower than the observed value. Using photoionization grids incorporating both stellar spectra and HMXB models (S20), we checked that our derived  $\log(L_{X,0.5-8 \text{ keV}}/\text{SFR}) \sim 40.9$  corresponds to  $\text{HeII}/\text{H}\beta$  values  $\sim 9$ –58 times lower than the integrated value of  $\text{HeII}/\text{H}\beta$  measured in IZw18 (K16). Finally, we report for the first time a substantial spatial separation ( $\approx 200 \text{ pc}$ ) between the HMXB and HeII emission peak.

Although a direct constraint to the  $Q(\text{HeII})$  produced by an HMXB in extremely metal-poor galaxies, such as IZw18, has not yet been reported, and one cannot rule out the contribution of X-rays to the  $\text{He}^+$  ionization there, all the points above argue against the HMXB being the main source responsible for the bulk of the nebular HeII emission in IZw18. Recent findings obtained by stacking the X-ray emission of HeII-emitting SF galaxies at  $z \sim 3$ , discard X-ray binaries as the dominant producers of  $\text{He}^+$  ionizing photons in distant SF galaxies (Saxena, et al. 2020). Along with the detailed study of the temporal variations and high-resolution mapping of the X-ray emission in IZw18 presented here, these stud-

ies highlight that the main source of HeII ionization is still puzzling both in nearby and distant SF systems (see also K15; K18).

#### ACKNOWLEDGEMENT

We thank the referees for helpful comments and suggestions. This work has been partially funded by projects AYA2016-79724-C4-4-P and PID2019-107408GB-C44 from the Spanish PNAYA. C.K., M.A.G., and J.V.M. acknowledge financial support from the State Agency

for Research of the Spanish MCIU through the ‘‘Center of Excellence Severo Ochoa’’ award to the Instituto de Astrofísica de Andalucía (SEV-2017-0709). M.A.G. acknowledges support from MCIU grant PGC2018-102184-B-I00 co-funded with FEDER funds. G.R.-L. acknowledges support from CONACyT (grant 263373) and PRODEP (México). This research has made use of data and/or software provided by the High Energy Astrophysics Science Archive Research Center (HEASARC), which is a service of the Astrophysics Science Division at NASA/GSFC.

#### REFERENCES

- Aloisi A., et al., 2007, *ApJ*, 667, L151  
 Asplund M., et al., 2009, *ARA&A*, 47, 481  
 Berghea, C. T. & Dudik, R. P. 2012, *ApJ*, 751, 104  
 Brorby M., et al., 2016, *MNRAS*, 457, 4081  
 Brown T. M., et al., 2002, *ApJ*, 579, L75  
 Cassata P., et al., 2013, *A&A*, 556, A68  
 de Mello D. F., et al., 1998, *ApJ*, 507, 199  
 Dunne, B. C., Points, S. D., & Chu, Y.-H. 2001, *ApJS*, 136, 119  
 Eldridge J. J., et al., 2017, *PASA*, 34, e058  
 Fruscione A., et al. 2006, *Proc. SPIE*, 62701V  
 Gabriel, C., Denby, M., Fyfe, D. J., et al. 2004, *Astronomical Data Analysis Software and Systems (ADASS) XIII*, 759  
 Garnett D. R., et al., 1991, *ApJ*, 373, 458  
 Gierliński, M., Done, C., & Page, K. 2009, *MNRAS*, 392, 1106  
 Götzberg Y., et al., 2018, *A&A*, 615, A78  
 Guseva N. G., Izotov Y. I., Thuan T. X., 2000, *ApJ*, 531, 776  
 Gutiérrez C. M., Moon D.-S., 2014, *ApJL*, 797, L7  
 HI4PI Collaboration, Ben Bekhti, N., Floer, L., et al. 2016, *A&A*, 594, A116  
 Heap S. R., Hubeny I., Lanz T. M., 2019, *ASPC*, 519, 267  
 Jaskot A. E., et al. 2011, *ApJ*, 729, 28  
 Kaaret P., Ward M. J., Zezas A., 2004, *MNRAS*, 351, L83  
 Kaaret, P., & Feng, H. 2013, *ApJ*, 770, 20  
 Kehrig C., et al., 2015, *ApJL*, 801, L28  
 Kehrig C., et al., 2016, *MNRAS*, 459, 2992  
 Kehrig C., et al., 2018, *MNRAS*, 480, 1081  
 Kehrig C., et al., 2020, *MNRAS*, 498, 1638  
 Kennicutt R. C., 1998, *ApJ*, 498, 541  
 Kubátová B., et al., 2019, *A&A*, 623, A8  
 Leboutteiller V., et al., 2017, *A&A*, 602, A45  
 Lelli F., et al. 2012, *A&A*, 537, A72  
 Mainali R., et al., 2018, *MNRAS*, 479, 1180  
 Martin, C. L. 1996, *ApJ*, 465, 680  
 Nazé Y., et al., 2003, *A&A*, 408, 171  
 Ponnada S., Brorby M., Kaaret P., 2020, *MNRAS*, 491, 3606  
 Prestwich A. H., et al., 2013, *ApJ*, 769, 92  
 Roth M. M., et al., 2005, *PASP*, 117, 620  
 Saxena A., et al., 2020, *MNRAS*, arXiv:2003.13800  
 Schaerer D., Fragos T., Izotov Y. I., 2019, *A&A*, 622, L10  
 Senchyna P., et al., 2017, *MNRAS*, 472, 2608  
 Senchyna P., et al., 2020, *MNRAS*, 494, 941  
 Stanway E. R., Eldridge J. J., 2019, *A&A*, 621, A105  
 Thuan T. X., et al., 2004, *ApJ*, 606, 213  
 Thuan T. X., Izotov Y. I., 2005, *ApJS*, 161, 240  
 Tumlinson J., Shull J. M., 2000, *ApJ*, 528, L65  
 Visbal E., Haiman Z., Bryan G. L., 2015, *MNRAS*, 450, 2506  
 Yoon S.-C., Dierks A., Langer N., 2012, *A&A*, 542, A113